

## LETTER

# High-security photoacoustic identity recognition by capturing hierarchical vascular structure of finger

Mingman Sun<sup>1,2</sup> | Yuanzheng Ma<sup>1,2</sup> | Zhuangzhuang Tong<sup>1,2</sup> |  
Zhiyang Wang<sup>1,2</sup>  | Wuyu Zhang<sup>1,2</sup> | Sihua Yang<sup>1,2\*</sup>

<sup>1</sup>MOE Key Laboratory of Laser Life Science and Institute of Laser Life Science, College of Biophotonics, South China Normal University, Guangzhou, China

<sup>2</sup>Guangdong Provincial Key Laboratory of Laser Life Science, College of Biophotonics, South China Normal University, Guangzhou, China

### \*Correspondence

Sihua Yang, MOE Key Laboratory of Laser Life Science & Institute of Laser Life Science, College of Biophotonics, South China Normal University, Guangzhou 510631, China.  
Email: yangsh@scnu.edu.cn

### Funding information

National Natural Science Foundation of China, Grant/Award Numbers: 11774101, 61627827, 61822505; Science and Technology Planning Project of Guangdong Province, China, Grant/Award Number: 2015B020233016; Science and Technology Program of Guangzhou, Grant/Award Number: 2019050001

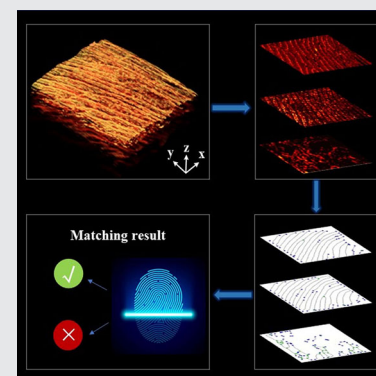
### Abstract

Currently, most biometric methods mainly use single features, making them easily forged and cracked. In this study, a novel triple-layers biometric recognition method, based on photoacoustic microscopy, is proposed to improve the security of biometric identity recognition. Using the photoacoustic (PA) dermoscope, three-dimensional absorption-structure information of the fingers was obtained.

Then, by combining U-Net, Gabor filtering, wavelet analysis and morphological transform, a lightweight algorithm called photoacoustic depth feature recognition algorithm (PADFR) was developed to automatically realize stratification (the fingerprint, blood vessel fingerprint and venous vascular), extracting feature points and identity recognition. The experimental results show that PADFR can automatically recognize the PA hierarchical features with an average accuracy equal to 92.99%. The proposed method is expected to be widely used in biometric identification system due to its high security.

### KEYWORDS

biometric recognition, finger vascular structure, feature recognition algorithm, photoacoustic microscopy



## 1 | INTRODUCTION

Biometric-based personal identification technology including fingerprinting and face recognition is the basis of information security, and also a hot issue in the field of biomedical engineering and artificial intelligence [1, 2]. Although biometric authentication technology is stable and accurate in recognition, it confronts a common problem—fraud or theft [3]. For example, fingerprint can be acquired from an object surface or through violence, which can spoof the fingerprint identification system [4]. Similarly, the frontal face photo is

easily acquired from secret camera, video, and even facial plastic surgery. Therefore, it is necessary to find an effective way to reduce the risk caused by fake biometric, especially for the personal identification in some sensitive places (e.g., bank, jail, and airport) [5]. Currently, near-infrared imaging of finger or palm vein network was proposed as a popular biometric authentication mode [6]. But due to the strong scattering of tissues, vein images usually have low signal-to-noise ratio (SNR) and low resolution, which makes it complex for post processing. Meanwhile, since the vein network is relatively simple and the diameter of vessel is

large, near-infrared imaging biometric authentication has faced various threats and attacks from artificially forged venous images, suggesting that single biological authentication is not safe.

Previous studies were proposed to use the dual authentication mode combining features of fingerprint and veins to carry out biometric identification [7]. Due to the limitation of tissue light scattering characteristics, the penetration depth of the conventional optical imaging is limited, which makes it difficult to obtain the blood vessel information of the deep layer of the finger. Doppler ultrasound [8] and near-infrared imaging [6] can obtain deep blood vessel information, but extracting fingerprints on the surface of the finger and achieving high-performance blood vessel imaging are difficult for them. Therefore, an effective imaging method for acquiring features of both fingerprint and veins, which can maintain good resolution at depth, is needed.

Photoacoustic microscopy (PAM) is a hybrid imaging technique with the advantages of the optical high-contrast and the ultrasonic deep penetration [9–20]. In view of the strengths of the spectroscopic-based specificity, PAM can offer label-free high-resolution imaging of melanin and hemoglobin at the depth of several

millimeters inside tissue [21–28]. Here, a triple biometric pattern method based on PA imaging was proposed for the first time. In this study, we obtained three-dimensional (3D) absorption-structure information of the fingers with the help of the photoacoustic dermoscope (PAD). During the experiment, subjects placed their fingers directly on top of the imaging window. After scanning, the 3D image of the finger was layered using Time-of-Flight (ToF). Besides, a new feature extraction algorithm including U-Net based on feature extraction, Gabor filter and features recognizing filter, was also developed, which is suitable for three-layer network processing [29]. After statistical analysis of triple-layers biometric recognition, we obtained high authentication accuracy and robustness.

## 2 | MATERIAL AND METHODS

The proposed triple-layers biometric recognition method consists of two modules: PA sensing hardware and PA identity recognition process. As shown in Figure 1, the sensing hardware system is based on PAD developed in our previous work in 2020 [30]. The PA signal excitation

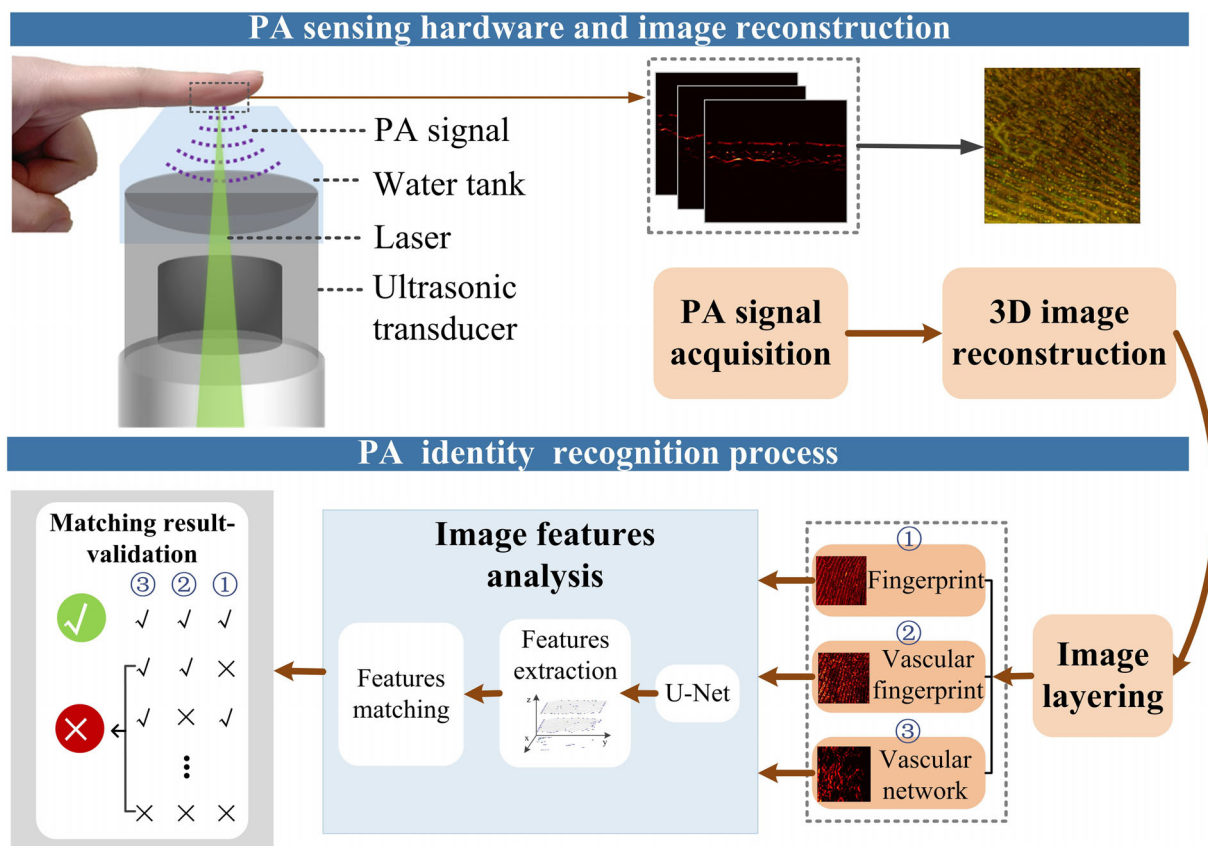


FIGURE 1 Framework of the triple-layers biometric recognition method, which consists of two modules: photoacoustic (PA) sensing hardware and PA identity recognition process

source is a pulsed laser (DTL-314QT, Laser-export), operating at wavelength of 532 nm with  $\sim 7$  ns duration and repetition rate of 10 kHz. Through the spatial filter system (KT310/M, Thorlabs), a Gaussian beam is produced and coupled into a single-mode fiber (460HP, Thorlabs) by a fiberport coupler (PAF-X-7-A, Thorlabs). Then, the fiber guides the laser into a 2D-scanner (LS2-25 T, Jiancheng Optics) probe. After the laser propagates through the single mode fiber, it was collimated by a fiber collimator (F240FC-532, Thorlabs, NA = 0.51), and then the laser beam was focused by aspheric lens (AL1225H, Thorlabs, NA = 0.20) to illuminate the sample. The subject's fingers are placed on the top of a water tank, which is filled with deionized water and encapsulated by thin film. The laser synchronizes the scanning and data acquisition systems. The linear motor drives the scanning system and the receiving system together, and moves at an adjustable speed which depends on the experimental requirements. The PA signals, received by a self-made ultrasonic transducer, are amplified by an amplifier (50 dB gain, LNA-650, RF Bay, USA) and digitized with a data acquisition card (M3i.3221, Spectrum) at a sampling rate of 200 MS/s. The acquired PA data are stored by a LabVIEW program for post image reconstruction.

The PADFR algorithm was used to extract features, which consists of the following steps (as shown in Figure 2). First, the image layering step is based on Time-of-Flight (ToF) of an A-line signal. By setting the vector  $V = [l_1, l_2, l_3]$  (in refers to the start point of each layer) empirically, the 3D images were divided into three layers. In the image layering process, we choose  $V = [2, 22, 72]$ . Second, the layered images are segmented by the pre-trained U-Net proposed by Dr. Olaf Ronneberge [29], and

the U-Net was refined by using our own dataset (20 samples) for transfer learning [31]. Due to the limitation of scanning speed, the photoacoustic fingerprint with obvious features was difficult to be extracted under the current system performance. After repeated experiments, 20 groups of photoacoustic vascular fingerprints with obvious features were selected for feature extraction. It was not enough to use 20 groups of data for deep learning training. The pre-trained U-Net was used [29]. The U-Net was obtained by using 60 groups of retinal blood vessels for vascular stratification training. With the help of such a network model of pre-training, samples based on transfer learning were obtained to reduce the training difficulty. After the completion of the training, three groups of remaining photoacoustic vascular fingerprint were selected for the test. The mean square error (MSE) of the fingerprint, blood vessel fingerprint and venous vascular between real value and after U-Net processing were 0.2422, 0.2768 and 0.1792. Third, the Gabor filter was used to remove noises. In order to use Gabor filter, the overall frequency and orientation of need to be obtained at first. And they were calculated by wavelet analysis and sobel filtering, respectively [32]. In the fourth step, morphology transform in OpenCV including opening-and-closing operation was used to find the mask of region of interest (ROI). This is practical in image processing for denoising. The skeletons of the images were extracted by using morphology operation *skimage.morphology.skeletonize* in Python. Last, by employing a  $3 \times 3$  operator, the number of changes of each point in the skeleton image with its neighboring points was calculated. If the number of neighboring changes around object pixel is equal to 2, this pixel is an endpoint, and if the number is equal

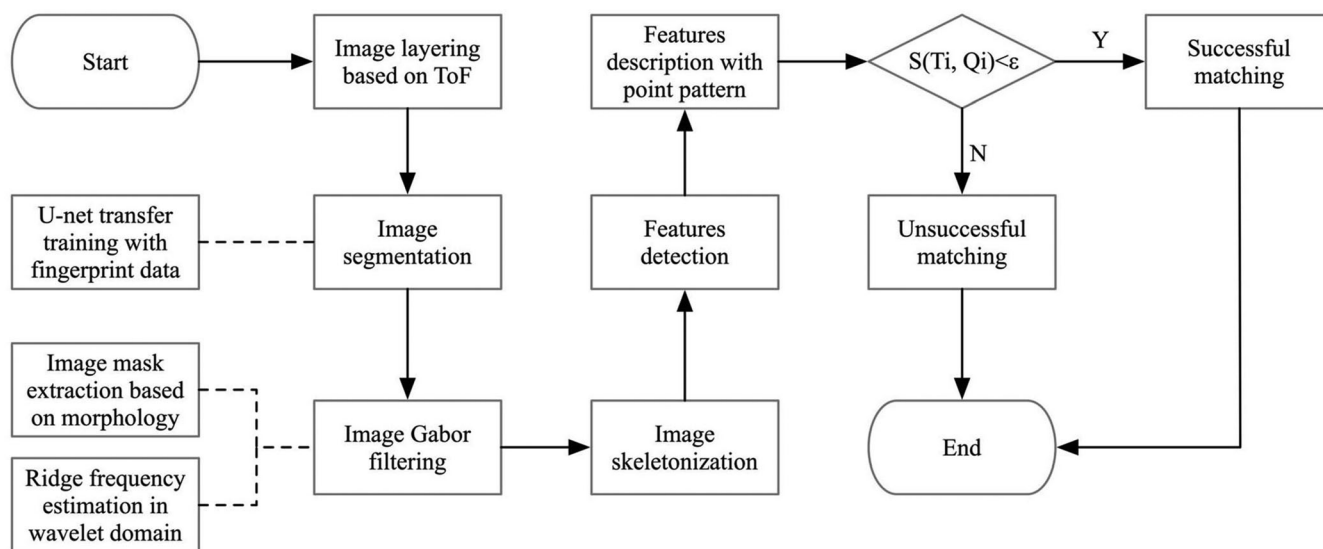


FIGURE 2 Flow diagram of the image features extraction and matching

to 6, it is a bifurcation. And all of these features are labeled on the graph. At the same time, the whorls were also captured and marked. These features are necessary for fingerprint identification and matching, which can be achieved by calculating the spatial distance (sd) and direction distance (dd) shown at Equation (1) [33]. Given two tolerance parameters  $r_o$  and  $\theta_o$  for error compensating, if the spatial distance (sd) and direction distance (dd) between the feature points of two images satisfy the Equation (1), then two images match successfully.

$$\begin{aligned} sd(m'_j, m_i) &= \sqrt{(x'_j - x_i)^2 + (y'_j - y_i)^2} \leq r_o \\ dd(m'_j, m_i) &= \min(|\theta_j - \theta_i|, 360 - |\theta_j - \theta_i|) \leq \theta_o \end{aligned} \quad (1)$$

### 3 | RESULTS

The PA images of the finger of one subject are shown in Figure 3. Figure 3A is a single frame from the 3D-rendered PA data and Figure 3B is a B-scan image along the depth direction with an imaging depth of about 1 mm. The epidermis, vascular fingerprints, and vessels were marked by yellow, green, and blue arrows

respectively in Figure 3A,B. In order to show the best results of TOF and verify the accuracy of the U-Net stratification results, here we adjusted the threshold to layer the 3D image. Based on Lambert–Beer law, laser decays exponentially as it enters the tissue, thus the deep signal is appropriately compensated empirically. Taking this signal as the reference layer, the upward tomographic layer was identified as the stratum corneum, and the downward tomographic layer was identified as the vascular villus layer and vascular layer. In this work, each B-scan image was composed of 500 A-line signals. After experimental testing, tomographic layer [1 to 2] were selected upward to be identified as the cuticle layer, tomographic layer [3 to 22] were selected downward to be identified as the vascular villus layer, and tomographic layer [23 to 72] were selected downward to identify as the vascular network layer. The depth-coded images of different depths are shown in Figure 3C-E. The range of the image is 5 mm × 5 mm. The length of B-scan was 5 mm. The scanning speed of the motor was 10 mm/s. A total of 500 B-scans were collected, so the time required for a single scan was about 250 s. Figure 3C shows the vascular fingerprint of the epidermal-dermal junction. In this region, we observe small absorbing spots arranged in a stripe pattern that are separated by approximately

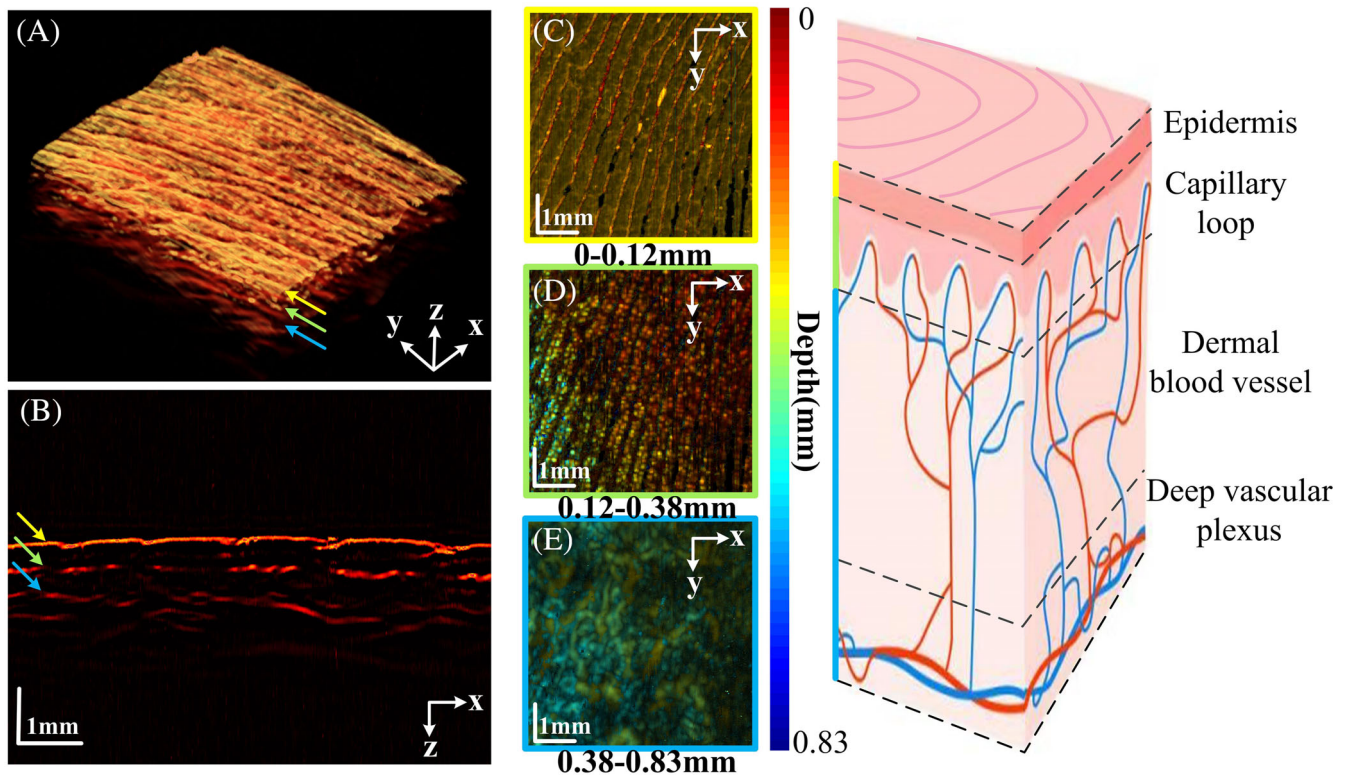


**FIGURE 3** In vivo imaging of human finger. A, 3D-finger image. B, The cross-sectional photoacoustic (PA) image of human finger. In A and B, the fingerprint, vascular fingerprints, and vessels were marked by yellow, green, and blue arrows, respectively. C-E, PA images of human finger at different depths. F, Diagram of skin layers and vascular network

0.9 mm, which is based on fingerprint distribution. Figure 3F presents a diagram of skin layers with corresponding vascular network. Each panel is integrated over a certain depth range, showing the epidermis (yellow frame), the dermal papillae with vascular fingerprints (green frame), and the dermis with deep vascular plexus (blue frame).

The schematic diagram of image features extraction and analysis are shown in Figure 4. Figure 4A shows PA images of fingerprint, vascular fingerprint and vascular network after multi-layered decomposition. The distribution of vascular fingerprints is consistent with fingerprints and the dermal papillae distribute in the position

of the fingerprint ridges. Figure 4B shows the images after U-Net processing for Figure 4A. It should be noted that the lines of vascular fingerprint images are smoother than fingerprint and have superior connectivity (the yellow arrows and red boxes) because fingerprints are easier to be damaged, which indicates high security. Figure 4C is the result of the morphological operation processing of Figure 4B, showing the masks of ROI. The images are more reasonable after further processing. For example, some wrongly identified breakpoints are reconnected, which was marked by circles. Figure 4 is the skeleton image of Figure 4C. The biometric features (contains endpoints, whorls and bifurcations) extracted images of

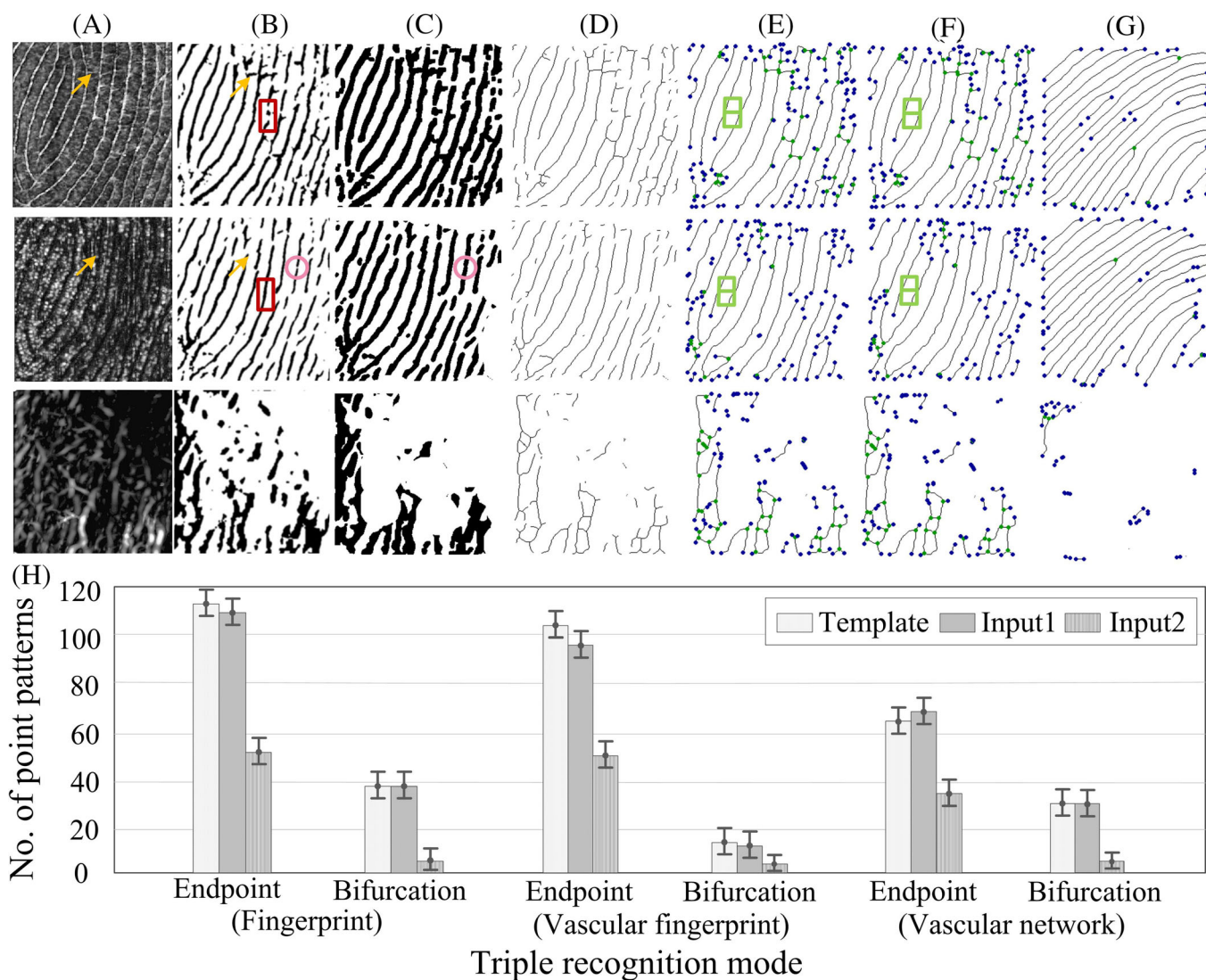


FIGURE 4 Schematic diagram of image features extraction and statistical analysis. The feature extraction process for Template is shown in A-E. A, Photoacoustic (PA) images after multi-layered decomposition. B, U-Net processed images of A. C, Morphological processed images of B. D, Skeleton extracted images of C. E, Biometric features (contains endpoints, whorls and bifurcations) extracted images of D. F, Biometric feature extraction images of the input images of Input 1. G, Biometric feature extraction images of Input 2. H, Feature statistics of the triple-layers biometric recognition method (fingerprint, vascular fingerprint and vascular network) for the Template and Input 1, as well as the Input 2

(d) are shown in Figure 4E. The endpoint was indicated by a blue dot, the bifurcation point was indicated by a green dot, and the whorl was marked by a green grid. The feature extraction process of Template (subject 1) is shown in A-E. The biometric feature extraction images of the input images of Input 1 (subject 1) are shown in Figure 4F and the biometric feature extraction images of Input 2 (subject 2) are shown in Figure 4G. The feature statistics of the triple recognition mode (fingerprint, vascular fingerprint and vascular network) for the Template, Input 1, and Input 2, are shown in Figure 4H. Due to the influence of dust and other factors, it can be seen that the features of the Input 1 are not exactly the same as those of the template. In addition, through the comparison of Input 1 and Input 2, it can be seen that the features of the same part of fingers of different people are different. The basic error formula for the preliminary calculation was used to calculate accuracy. The total number of features of Template (A) and Input 1 (B) were counted. Then the equation below was used to calculate the relative error (RE) and accuracy of the set of data.

$$\text{Accuracy} = \left(1 - \frac{B-A}{A}\right) \times 100\% \quad (2)$$

By calculating five groups of input and stored data, the average accuracy of triple recognition achieves 92.99%. The average matching accuracy of each layer was also calculated. The average accuracy of fingerprint, vascular fingerprint and vascular network were 81.82%, 83.16% and 92.86%. The triple-layers biometric recognition method has greater number of eigenvalues than the single biometric recognition method and thus has higher accuracy.

## 4 | DISCUSSION AND CONCLUSIONS

Further efforts can be made to improve the triple-layers biometric recognition method. Due to the limitation of single point scanning motion by linear motor, the imaging speed is low. The imaging time can be shortened by fully use of linear array and an additional voice coil motor [34]. In addition, the whole imaging platform is still relatively bulky. To mitigate the setup, high-energy light-emitting diodes (LEDs) or laser diodes arrays which are smaller and possess higher energy efficiency than flashlamp-pumped lasers, can be used [35]. By using LEDs or laser diodes with high repetition frequency, the acquisition time can be reduced as well. Besides, it is necessary to display the results of identity recognition in real time. Real-time imaging methods such as array imaging and deep learning decoder can fill this gap. At the same time, there were some

recognition errors in the algorithm process, which can be compensated by multiple acquisitions. The future algorithm is not only based on KNN classification recognition [36], but also can further improve the accuracy by using deep learning fingerprint recognition. Overall, the triple-layers biometric recognition method will be complete by increasing the imaging speed to collect sufficient samples.

In conclusion, we have successfully implemented a new mode of biometric recognition. Compared with the single biometric recognition method, it has higher accuracy and security. By simply placing a finger above the imaging window, sufficient information of fingerprint and blood vessel can be obtained. The images of microvessels have a higher resolution than those by infrared imaging, which allows a more accurate view of vascular density. Because of the increasing demand for securer identification, the triple-layers biometric recognition method will have a broad application in various areas.

## ACKNOWLEDGMENTS

This research is supported by the National Natural Science Foundation of China (61822505; 11774101; 61627827;), The Science and Technology Planning Project of Guangdong Province, China (2015B020233016), Science and Technology Program of Guangzhou (2019050001).

## CONFLICT OF INTEREST

The authors declare that there are no conflicts of interest.

## DATA AVAILABILITY STATEMENT

The authors declare that there are no conflicts of interest.

## ORCID

Zhiyang Wang  <https://orcid.org/0000-0002-9262-2899>

## REFERENCES

- [1] G. Betta, D. Capriglione, M. Corvino, C. Liguori, A. Paolillo, *IEEE Trans. Instrum. Meas.* **2013**, *62*, 1008.
- [2] H. Sellahewa, S. A. Jassim, *IEEE Trans. Instrum. Meas.* **2010**, *59*, 805.
- [3] A. K. Jain, A. Ross, S. Prabhakar, *IEEE Trans. Circuits Syst. Video Technol.* **2004**, *14*, 4.
- [4] K. Y. T. Matsumoto, H. Matsumoto, S. Hoshino, *Proc. SPIE* **2002**, *4677*, 275.
- [5] A. Adesuyi, O. Oluwafemi, A. V. Rick, *J. Comput. Eng.* **2013**, *10*, 51.
- [6] L. Chen, J. Wang, S. Yang, H. He, *IEEE Trans. Instrum. Meas.* **2017**, *66*, 294.
- [7] A. Kumar, Y. Zhou, *IEEE Trans. Image Proc* **2012**, *21*, 2228.
- [8] A. Iula, A. Savoia, and G. Caliano, "3D ultrasound palm vein pattern for biometric recognition, in 2012 IEEE International Ultrasonics Symposium, Dresden, **2012**, 1–4.
- [9] L. V. Wang, S. Hu, *Science* **2012**, *335*, 1458.
- [10] J. Lv, Y. Peng, S. Li, Z. Guo, Q. Zhao, X. Zhang, L. Nie, *Eur. Radiol.* **2018**, *28*, 2176.

- [11] L. Xi, S. R. Grobmyer, L. Wu, R. Chen, G. Zhou, L. G. Gutwein, J. Sun, W. Liao, Q. Zhou, H. Xie, H. Jiang, *Opt. Express* **2012**, *20*, 8726.
- [12] M. Zhou, H. Zhao, H. Xia, J. Zhang, Z. Liu, C. Liu, F. Gao, *J. Biophotonics* **2019**, *12*, e201900042. <https://doi.org/10.1002/jbio.201900042>.
- [13] L. Xiang, B. Wang, L. Ji, H. Jiang, *Sci. Rep.* **2013**, *10*, 1038.
- [14] W. Qi, T. Jin, J. Rong, H. Jiang, L. Xi, *J. Biophotonics* **2017**, *10*, 1580.
- [15] V. Ntziachristos, J. Ripoll, L. V. Wang, R. Weissleder, *Nat. Biotechnol.* **2005**, *23*, 313.
- [16] F. Gao, X. Feng, Y. Zheng, *Appl. Phys. Lett.* **2014**, *104*, 213701.
- [17] Q. Zhao, R. Lin, C. Liu, J. Zhao, G. Si, L. Song, J. Meng, *J. Biophotonics* **2019**, *12*, e201800421. <https://doi.org/10.1002/jbio.201800421>.
- [18] F. Duan, H. Ma, J. Zhang, S. Li, H. Li, Z. Wu, F. Hong, L. Zeng, L. Nie, *Chin. Opt. Lett.* **2020**, *18*, 121701.
- [19] Y. Liu, Y. Yang, M. Sun, M. Cui, Y. Fu, Y. Lin, Z. Li, L. Nie, *Chem. Sci.* **2017**, *8*, 2710.
- [20] J. Lv, S. Li, J. Zhang, F. Duan, Z. Wu, R. Chen, M. Chen, S. Huang, H. Ma, L. Nie, *Theranostics* **2020**, *10*, 816.
- [21] M. Jeon, J. Kim, C. Kim, *Med. Biol. Eng. Comput.* **2016**, *54*, 283.
- [22] F. Yang, Z. Wang, W. Zhang, H. Ma, Z. Cheng, Y. Gu, H. Qiu, S. Yang, *J. Biophotonics* **2020**, *10*, 1002.
- [23] W. Huang, R. Chen, Y. Peng, F. Duan, Y. Huang, W. Guo, X. Chen, L. Nie, *ACS Nano* **2019**, *13*, 9561.
- [24] Z. Xie, S. Jiao, H. F. Zhang, C. A. Puliafito, *Opt. Lett.* **2009**, *34*, 1771.
- [25] W. Qin, W. Qi, T. Jin, H. Guo, L. Xi, *Appl. Phys. Lett.* **2017**, *111*, 263704.
- [26] L. Xi, H. Jiang, *Appl. Phys. Lett.* **2012**, *101*, 173702.
- [27] J. Yang, G. Zhang, Q. Shang, M. Wu, H. Jiang, *J. Biophotonics* **2020**, *10*, 1002.
- [28] Z. Cheng, H. Ma, Z. Wang, S. Yang, *Front. Optoelectron* **2020**, *13*, 307.
- [29] O. Ronneberger, P. Fischer, T. Brox, U-net: Convolutional networks for biomedical image segmentation. in Medical Image Computing and Computer-Assisted Intervention - MICCAI 2015 - 18th International Conference Munich, Germany, October 5–9, 2015, Proceedings, Part III, *Lecture Notes in Computer Science*, Vol. 9351 (Eds: N. Navab, J. Hornegger, W. Wells, A. Frangi), Springer, Munich, Germany, **2015**, p. 234.
- [30] Z. Wang, F. Yang, H. Ma, Z. Cheng, S. Yang, *J. Biophotonics* **2020**, *13*, 9.
- [31] T. Galanti, L. Wolf, T. Hazan, *Inform. Inference J. IMA* **2016**, *5*, 159.
- [32] J. Bo, T. H. Ping, X. M. Lan, *WSEAS Trans. Syst.* **2008**, *7*, 14531462.
- [33] S. Kivutinjeru, R. Oboko, *Int. J. Comput. Sci. Inf. Technol.* **2016**, *8*, 59.
- [34] L. Wang, K. Maslov, J. Yao, B. Rao, L. V. Wang, *Opt. Lett.* **2011**, *10*, 1364.
- [35] M. Schwarz, M. Omar, A. Buehler, J. Aguirre, V. Ntziachristos, *IEEE Trans. Med. Imag.* **2015**, *34*, 672677.
- [36] S. Yang, H. Jian, Z. Ding, H. Zha, C. L. Giles, *DBLP* **2007**, 4702, 248.

**How to cite this article:** M. Sun, Y. Ma, Z. Tong, Z. Wang, W. Zhang, S. Yang, *J. Biophotonics* **2021**, e202100086. <https://doi.org/10.1002/jbio.202100086>